Journal of Zhejiang University-SCIENCE A (Applied Physics & Engineering)
ISSN 1673-565X (Print); ISSN 1862-1775 (Online)
www.jzus.zju.edu.cn; www.springerlink.com
E-mail: jzus@zju.edu.cn

Local heat transfer enhancement induced by a piezoelectric fan in a channel with axial flow*

Yun-long QIU, Chang-ju WU†‡, Wei-fang CHEN

School of Aeronautics and Astronautics, Zhejiang University, Hangzhou 310027, China

†E-mail: wuchangju@zju.edu.cn

Received Feb. 14, 2020; Revision accepted May 22, 2020; Crosschecked Nov. 16, 2020

Abstract: The present work experimentally and numerically investigates the local heat transfer enhancement induced by a piezoelectric fan interacting with a cross flow in a local heated channel. The piezoelectric fan is placed along the flow direction and tested under different amplitudes and flow rates. In the simulations, a spring-based smoothing method and a local remeshing technique are used to handle the moving boundary problems. Hybrid mesh is used to reduce the size of dynamic mesh domain and to improve computational efficiency. The experimental and numerical values of the time-averaged mean Nusselt number are found to be in good agreement, with deviations of less than 10%. The experimental result shows that the heat transfer performance of the heated surfaces is substantially enhanced with a vibrating piezoelectric fan. The numerical result shows that the heat transfer enhancement comes from the strong longitudinal vortex pairs generated by the piezoelectric fan, which significantly promote heat exchange between the main flow and the near-wall flow. In the case of a=0.66 (a is the dimensionless amplitude) and Re=1820, the enhancement ratio of the time-averaged mean Nusselt number reaches 119.9%.

Key words: Piezoelectric fan; Local heat transfer enhancement; Forced convection; Longitudinal vortex; Pressure drop
https://doi.org/10.1631/jzus.A2000057 **CLC number:** TK01

1 Introduction

The rapid growth of heat flux in electronic systems has made thermal management very important. However, the effectiveness of conventional natural and forced convection cooling methods is in general limited by space and noise constraints. Therefore, in order to improve convection heat transfer performance, many assistive technologies have been proposed over the past decades, including nanofluids (Wang and Mujumdar, 2007; Wen et al., 2009; Ghalambaz et al., 2019a, 2019b, 2020), geometry optimization (Peles et al., 2005; Kurnia et al., 2011; Lee et al., 2015; Alsabery et al., 2019), synthetic jets (Deng et al., 2019; Xu et al., 2019; Arshad et al., 2020), and oscillating insertions (Yeom et al., 2016; Ghalambaz et al., 2017; Jamesahar et al., 2020). Among these new technologies, the piezoelectric fan has attracted extensive attention because of its unique features such as high reliability, low noise, low power consumption, and minimum space requirement (Hales and Jiang, 2018). This innovative design consists of a piezoelectric layer and a flexible blade. When an alternating voltage is applied to the piezoelectric layer, the piezoelectric layer expands and contracts periodically, which causes vibration of the flexible blade. This vibration has two influences on the surrounding fluid: (1) pushing the fluid near the fan tip and generating pseudo-jets; (2) causing rotation of the surrounding fluid and the formation of large-scale vortexes.

‡ Corresponding author
* Project supported by the National Natural Science Foundation of China (Nos. 51575487 and 51875521)
ORCID: Yun-long QIU, https://orcid.org/0000-0002-2873-743X; Chang-ju WU, https://orcid.org/0000-0002-7423-3371

Over the past few decades, the ability of the piezoelectric fan to generate pseudo-jet flows has been widely studied for its feasibility to replace the rotary fan in space- or weight-restricted heat transfer applications. Açikalin et al. (2004, 2007) studied the heat transfer enhancement induced by the jet-like air flow generated by a piezoelectric fan, and found the fan amplitude and the frequency offset from the first resonant frequency to be two critical parameters for the cooling capability of such fans. Liu et al. (2009) investigated the effects of fan arrangement, and found that the cooling performance for horizontal and vertical arrangements had the same order of magnitude but different distributions. Abdullah et al. (2009) analyzed the effect of fan height on the heat transfer performance of piezoelectric fans. The result showed that the heat transfer enhancement was insensitive to the fan height. Wait et al. (2007) and Fairuz et al. (2014) studied the flow characteristics of piezoelectric fans working at higher resonant modes. They demonstrated that the advantages of operating at higher resonant modes became less prominent because power consumption increased and the generated air flow decreased. Kimber and Garimella (2009) and Sufian et al. (2013) tested the cooling performance of a piezoelectric fan array on a heated surface. The results indicated that the heat transfer performance of a fan array was better than that of a single fan. Abdullah et al. (2012a, 2012b) and Ma et al. (2012) combined a piezoelectric fan with a heat sink and evaluated the thermal performance. The effects of tip gap, fan amplitude, and orientation angle were investigated. The results showed that the best cooling performance was achieved at the least tip gap and the highest amplitude with a vertical orientation.

Although natural convection heat transfer performance can be enhanced up to several times by the effect of the pseudo-jet flow generated by a piezoelectric fan, it is still far from meeting the high-heat-flux heat removal requirements of high-performance electronic equipment. Considering that forced convection heat transfer technology with the presence of a cross flow has a much higher cooling capability, it is important to investigate the vortex generating ability of a piezoelectric fan and to use it as an assistive device for cooling high-performance electronic equipment.

Among these previous studies on vortex generating characteristics of piezoelectric fans, Lin (2013) investigated the cooling capability of a piezoelectric fan on a heated cylinder under a forced convection condition, and found that the vortexes generated by the vibrating fan promoted mixing in the mainstream and slightly enhanced the heat transfer of the cylinder. Jeng and Liu (2015) studied the influence of cross flow on the fluid and thermal behaviors of the heat sink with an upstream vertically-oriented piezoelectric fan, and found that the piezoelectric fan's vibration strengthened momentum exchange in the cross flow at low Reynolds number and enhanced the heat transfer performance of the heat sink. Li et al. (2017, 2018a, 2018b) investigated the heat transfer performance of a heated surface in the affected region of a vertically-oriented piezoelectric fan interacting with a cross flow. The result showed that the heat transfer enhancement induced by the impinging jet-like air flow was obviously weakened under the effect of cross flow, but the heat transfer performance in the downstream region was greatly enhanced due to the entrainment effect of the shedding vortexes.

The literature mentioned above illustrates that a vertically-oriented piezoelectric fan interacting with a cross flow can significantly enhance the heat transfer performance of heated surfaces, but the vertical arrangement also requires extra space for installation and that obviously limits its application. In order to solve this problem, we propose here a horizontal arrangement for installing a piezoelectric fan interacting with cross flow in a channel. The horizontal arrangement not only has an excellent heat transfer performance, but also does not need extra installation space. It is therefore a better choice in space-restricted forced-convection heat transfer applications, such as cold plate.

2 Experimental

2.1 Experimental setup

The experimental setup mainly consists of a pressure supply system, a test section, and a data acquisition system, as schematically illustrated in Fig. 1. The pressure supply system is composed of a vacuum pump, a vacuum tank, a shutoff valve, a pressure reducing valve, a flowmeter with an accuracy of 0.3 L/min, and a gas filter. The flow rate of the channel is set from 20 to 40 L/min (Re=910–1820, Re is the Reynolds number) by adjusting the pressure reducing valve.

2.2 Test section

As shown in Fig. 2, the test section is composed of a piezoelectric fan system, a copper block, and a heating system. The channel is 30 mm high, 20 mm wide, and 450 mm long with dimension error of 0.2 mm. Three 150-mm long heated surfaces are located at the middle of the channel. A horizontally-oriented piezoelectric fan is positioned upstream of the heated surfaces along the main stream. The upstream side of the piezoelectric fan is fixed.

The heat sink design and the working fluid air are used to achieve an approximate isothermal boundary condition for the heat transfer surfaces. Compared with the uniform heat flux boundary condition, the isothermal boundary condition has the following advantage: for the unsteady heat transfer problem, the fluid-solid conjugate heat transfer should be considered in simulations when the uniform heat flux boundary condition is used; otherwise, the temperature of the heat transfer surfaces would have a severe synchronous fluctuation with the piezoelectric fan if the fluid domain only was computed. However, for the isothermal boundary condition, if the heat capacity of the solid part is large enough, the time required for temperature change of the copper block is much longer than the vibration period of the piezoelectric fan, so that the temperature of the solid domain remains nearly unchanged in a vibration period of the piezoelectric fan.

The steady design of the test section has two major benefits: (1) it is much easier to measure the time-averaged mean heat transfer coefficient and (2) the solid domain can be neglected in simulations, which greatly improve the computational efficiency.

The heating system is composed of a direct current (DC) power supply and a cartridge heater. The cartridge heater is installed at the lower part of the copper block with a constant power of 10 W. The value of Gr/Re^2 is kept less than 0.1 to ensure the effect of natural convection is negligible (Gr is the Grashof number). To measure temperature distributions, 25 T-type thermocouples with an accuracy of 0.2 °C are installed under the heat transfer surfaces with a lateral interval of 13 mm and a longitudinal interval of 30 mm. These thermocouples are connected to a computer thermocouple via a data acquisition card. The copper block and the unheated surfaces of the channel are enclosed with thick polyurethane foam insulation to reduce heat loss.

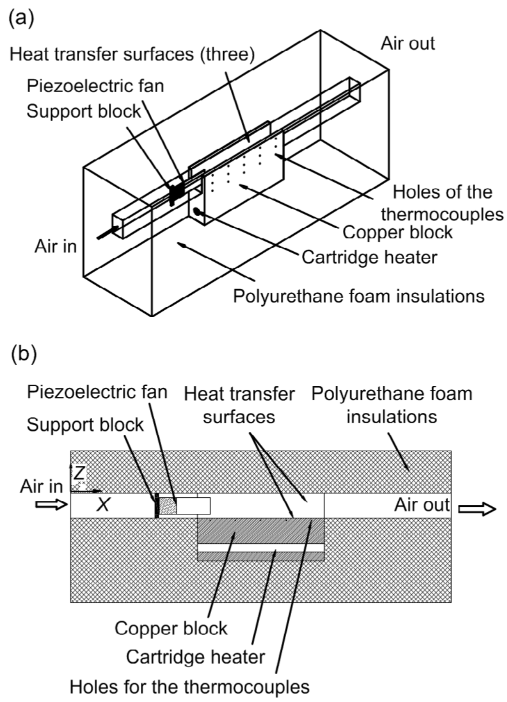

Fig. 2 Schematic diagrams of the test section
(a) Perspective view, (b) Cross-section view

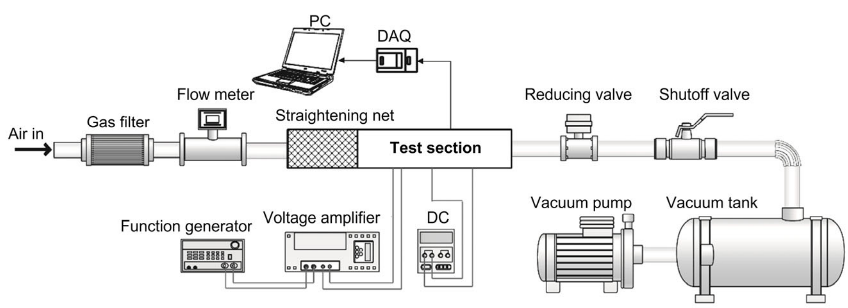

Fig. 1 Schematic diagram of the experimental setup
DAQ: data acquisition

The piezoelectric fan is composed of a thin blade (FR4) attached to a patch of piezoelectric material. The structure of the piezoelectric fan is plotted in Fig. 3. The fixed area of the piezoelectric fan is stuck to a 1-mm thick and 4-mm wide support block to achieve horizontal installation. Dimensions and specifications of the piezoelectric fan are listed in Table 1.

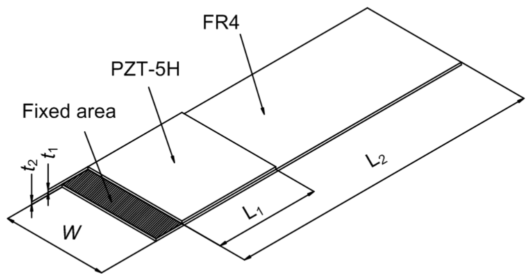

Fig. 3 Schematic diagram of the piezoelectric fan

Table 1 Dimensions and specifications of the piezoelectric fan

Parameter	Value
Thickness of PZT-5H, t_1 (mm)	0.2
Thickness of FR4, t_2 (mm)	0.2
Width of fan, W (mm)	20.0
Length of PZT-5H, L_1 (mm)	20.0
Length of fan, L_2 (mm)	60.0
First-order resonant frequency, f (Hz)	41.2

In the current experiment, the piezoelectric fan is working at its first resonant mode to achieve large amplitude, and it is tested under different voltages and flow rates to study the effects of amplitude and cross flow Reynolds number on the cooling capability of the piezoelectric fan.

2.3 Parameter definitions

The cross flow Reynolds number (Re) of the channel is defined as

$$Re = \frac{\rho u_{\mathrm{in}} D_{\mathrm{h}}}{\mu}, \tag{1}$$

where D_{h} and u_{in} represent the hydraulic diameter and the inlet velocity, respectively. ρ and μ represent air density and air viscosity, respectively.

The dimensionless amplitude (a) of the piezoelectric fan is expressed as

$$a = \frac{A_{\mathrm{pp}}}{D_{\mathrm{h}}}, \tag{2}$$

where A_{pp} is the peak to peak vibration amplitude of the piezoelectric fan.

The actual heat power P_{e} transferred into the working fluid can be calculated as follows:

$$P_{\mathrm{e}} = \dot{m} c_{\mathrm{p}} (T_{\mathrm{out}} - T_{\mathrm{in}}), \tag{3}$$

where $\dot{m}$ is the mass flow rate of the channel. T_{in} and T_{out} are the inlet and outlet mean temperatures, respectively. c_{p} is the specific heat capacity of air. To eliminate the physical property difference of the incoming flow, T_{in} is kept at 288.15 K.

The mean heat transfer coefficient ($\overline{h}$) of the heated surfaces is obtained:

$$\overline{h} = \frac{\dot{m} c_{\mathrm{p}} (T_{\mathrm{out}} - T_{\mathrm{in}})}{A \cdot \Delta T_{\mathrm{lmtd}}}, \tag{4}$$

where A is the area of those surfaces. ΔT_{lmtd} is the log mean temperature difference of the channel and is given as

$$\Delta T_{\mathrm{lmtd}} = \frac{(\overline{T}_{\mathrm{m}} - T_{\mathrm{in}}) - (\overline{T}_{\mathrm{m}} - T_{\mathrm{out}})}{\ln[(\overline{T}_{\mathrm{m}} - T_{\mathrm{in}}) / (\overline{T}_{\mathrm{m}} - T_{\mathrm{out}})]}, \tag{5}$$

where $\overline{T}_{\mathrm{m}}$ is the mean temperature of the heat transfer surfaces. As the working fluid is air and the hydraulic diameter is large, the heat conduction thermal resistance between the thermocouples and the heat transfer surfaces is far less than the heat convection thermal resistance of the heat transfer surfaces. Therefore, it is reasonable to use the measurements of the thermocouples to calculate ΔT_{lmtd}.

According to the test results, the temperature of the heat transfer surfaces is evenly distributed. The maximum of the ratio $(T_{\mathrm{m},i} - T_{\mathrm{m},j}) / (\overline{T}_{\mathrm{m}} - T_{\mathrm{in}})$ is less than 2%. In addition, the thermocouple measurements remain almost unchanged during the vibration period of the piezoelectric fan, and thus the mean heat transfer coefficient ($\overline{h}$) calculated by Eq. (4) can be considered as the time-averaged mean heat transfer coefficient in one fan vibration period.

The definition of the time-averaged mean Nusselt number ($\overline{Nu}$) is given as

$$\overline{Nu} = \frac{\bar{h}D_\mathrm{h}}{k}, \tag{6}$$

where k is the thermal conductivity of air and is calculated based on the bulk mean temperature.

The experimental uncertainties of the relevant parameters are calculated based on the method proposed by Moffat (1988). The maximum uncertainty of Re is ±1.7% and that of $\overline{Nu}$ is ±6.7%.

2.4 Experimental results

Fig. 4 shows the variations of the time-averaged mean Nusselt number ($\overline{Nu}$) with the dimensionless amplitude (a) for different Re. The result indicates that, for each Re-controlled data series, the time-averaged mean Nusselt number increases with the amplitude of the piezoelectric fan. Moreover, the benefits of rising amplitude for a>0.4 are more obvious at higher Re. The causes of the heat transfer enhancement and the effects of amplitude and cross flow Reynolds number on the heat transfer performance of the piezoelectric fan will be analyzed in Section 4, based on the numerical simulation results.

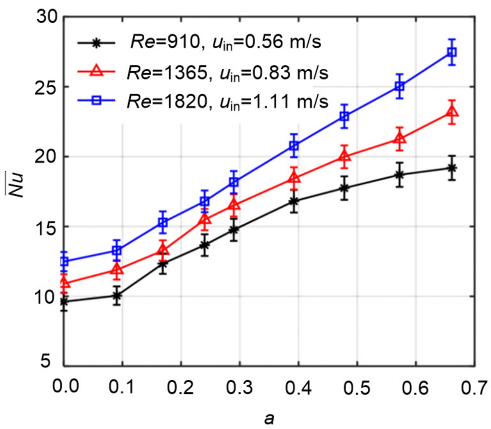

Fig. 4 Variations of the time-averaged mean Nusselt number with the dimensionless amplitude (*a*) for different *Re*

3 Numerical simulations

To explain the local heat transfer enhancement mechanism and analyze the effects of amplitude and cross flow Reynolds number, a series of simulations are performed to achieve numerical visualization and obtain the flow information. The finite volume method is used to perform a discrete solution for the governing equations. The spring-based smoothing method and the local remeshing technique are used to handle the moving boundary problems.

3.1 Governing equations

First, several assumptions are made to simplify the governing equation:

1. Flow is 3D and incompressible.

2. Physical properties of the working fluid are constants.

3. Effects of gravity, radiation, and viscous heating are neglected.

Based on the assumptions above, the universal form of the governing equations for the stationary cases can be expressed as

$$\frac{\partial(\rho u_i \phi)}{\partial x_i} = \frac{\partial}{\partial x_i}\left(\Gamma_\phi \frac{\partial \phi}{\partial x_i}\right) + S_\phi. \tag{7}$$

The specific forms of the symbols ϕ, Γ_ϕ, S_ϕ used in the governing equations are listed in Table 2. u_i is the velocity vectors and p is the relative pressure.

Table 2 Specific forms of the symbols used in the governing equations

Equation	ϕ	Γ_ϕ	S_ϕ
Continuity	1	0	0
Momentum	u_i	μ	$-\partial p/\partial x_i$
Energy	T	k/c_p	0

The physical properties of air used in the simulations are listed as follows:

$$\rho = 1.225\ \mathrm{kg/m^3},\ \ \mu = 1.79\times10^{-5}\ \mathrm{kg/(m\cdot s)},$$
$$k = 0.0254\ \mathrm{W/(m\cdot K)},\ \ c_\mathrm{p} = 1006\ \mathrm{J/(kg\cdot K)}.$$

Similarly, the universal form of the governing equations for the vibrating cases can be expressed as

$$\frac{\partial(\rho\phi)}{\partial t} + \frac{\partial(\rho(u_i - \hat{u}_i)\phi)}{\partial x_i} = \frac{\partial}{\partial x_i}\left(\Gamma_\phi \frac{\partial \phi}{\partial x_i}\right) + S_\phi, \tag{8}$$

where t is time, and $\hat{u}$ represents the velocity of the moving mesh.

As in previous numerical research on piezoelectric fans (Abdullah et al., 2012b; Lin, 2013; Sufian et al., 2013; Fairuz et al., 2014; Li et al., 2017), the k-ω based shear-stress-transport (SST) model is used to describe the turbulent flow for the vibrating cases in this study.

The governing equations are solved by an in-house computational fluid dynamics (CFD) solver based on the finite-volume method. The semi-implicit method for pressure linked equations consistent (SIMPLEC) algorithm is utilized for pressure-velocity coupling and the first-order implicit scheme is used for the unsteady term. The validity of the in-house solver has been verified in our previous work (Xia and Chen, 2016; Guo et al., 2018; Jiang et al., 2018).

3.2 Computational domain and boundary conditions

Fig. 5 shows the computational domain which consists of a piezoelectric fan and a rectangular channel with three heated surfaces in the middle part. The piezoelectric fan is simplified as a thin beam and the time-dependent displacement of every point on the vibrating beam is defined as

$$y(x)=\frac{A_{\mathrm{pp}}}{2}\cdot g(x)\cdot\sin(2\pi ft), \tag{9}$$

where $g(x)$ is the mode shape which is measured by a laser displacement sensor and described by a polynomial:

$$g(x)=-1.8865\mathrm{e}^{-7}x^4+2.1833\mathrm{e}^{-5}x^3-4.0447\mathrm{e}^{-4}x^2+3.0414\mathrm{e}^{-3}x-7.4908\mathrm{e}^{-4}. \tag{10}$$

Fig. 6 compares the fitting result of Eq. (10) and the test result. It shows that the maximum deviation of the correlation is less than 3%.

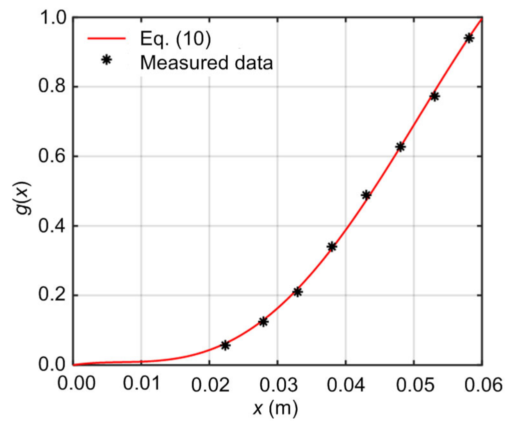

Fig. 6 Vibration mode shape of the piezoelectric fan

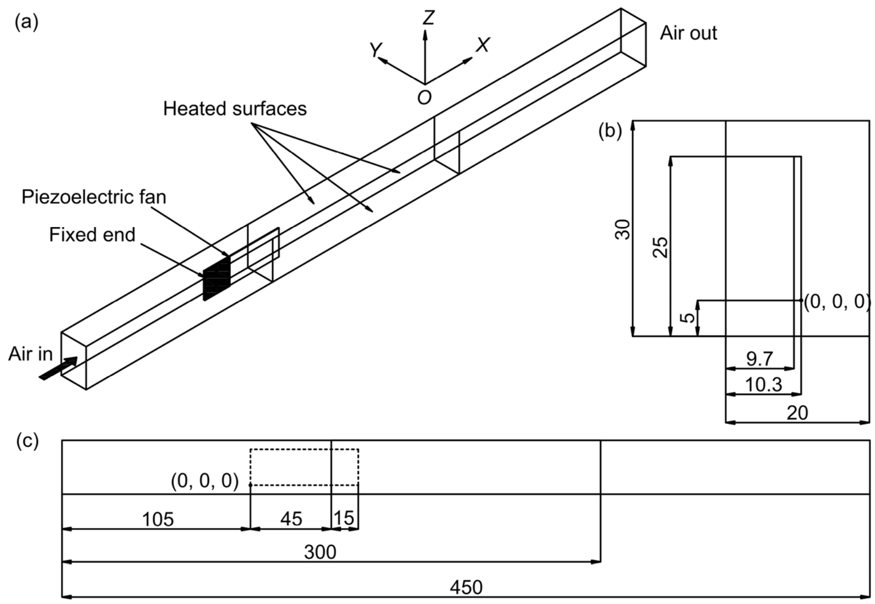

Fig. 5 Schematic of the computational domain (a); side view of the computational domain with a magnification of 5 (b); front view of the computational domain (c) (unit: mm)

The detailed boundary conditions on the surfaces of the computational domain are listed as follows:
On the channel inlet:

$$u=u_{\text{in}},\ v=w=0,\ T_{\text{in}}=288.15\ \text{K},$$

where u, v, and w represent the velocity components in X, Y, and Z directions, respectively.
On the channel outlet:

$$\frac{\partial T}{\partial n}=0,\ \ p=1.013\times 10^{5}\ \text{Pa},$$

where n represents the normal direction.
On the piezoelectric fan:

$$y(x)=\frac{A_{\text{pp}}}{2}\cdot g(x)\cdot\sin(2\pi ft),\quad \frac{\partial T}{\partial n}=0.$$

On the heated surfaces:

$$u=v=w=0,\ \ T_{\text{sur}}=\overline{T}_{\text{m}},$$

where T_{sur} is the temperature of the heated surfaces.
On the other walls of the channel:

$$u=v=w=0,\ \ \frac{\partial T}{\partial n}=0.$$

3.3 Mesh generation and independence validation

As seen in Fig. 7, the fluid domain is separated into two parts, namely, a static region and a dynamic region. A hybrid mesh is used to restrict the mesh deformation in the dynamic region with a tetrahedral mesh. The deformation and reconstruction of the dynamic mesh are controlled by the spring-based smoothing method and the local remeshing technique. The detailed steps are listed as follows:

1. Compute the flow field and temperature field in the whole computational domain.
2. Calculate the position of the moving boundary in the next time step by Eq. (9).
3. Use a spring-based smoothing method for mesh deformation.
4. Check the mesh quality after deformation. If the mesh quality is lower than the critical value, regenerate the mesh.
5. According to the geometrical relations between the old mesh and the new mesh, compute the physical quantities in the new mesh cells.

Fig. 8 compares the computational meshes before and after deformation. The result shows that the dynamic mesh is well-controlled and the mesh quality is acceptable.

Mesh-independence is tested for the case of a=0.48 and Re=1820. Fig. 9 shows the variations of the time-averaged mean Nusselt number with the total

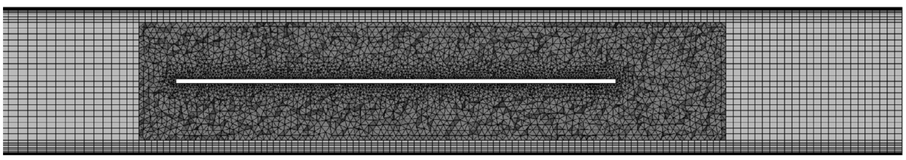

Fig. 7 Computational mesh using hybrid mesh

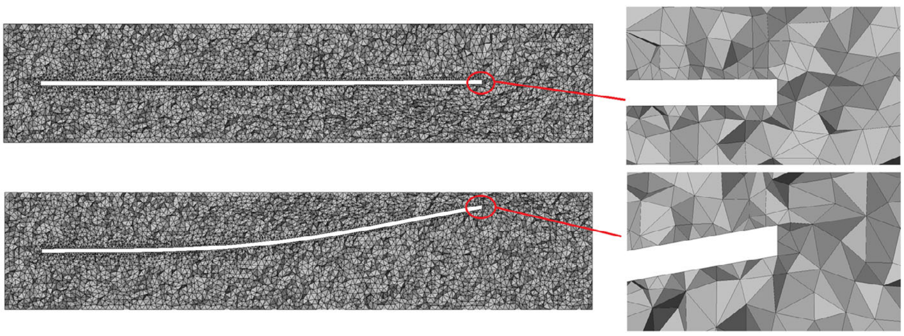

Fig. 8 Computational meshes before and after deformation

mesh number. For numerical simulations, the time-averaged mean Nusselt number is calculated by

$$\overline{Nu}=\frac{1}{\tau}\int_0^{\tau}\overline{Nu}(t)\mathrm{d}t=\frac{1}{\tau}\int_0^{\tau}\frac{\overline{q}(t)D_{\mathrm{h}}}{\Delta T_{\mathrm{lmtd}}(t)k}\mathrm{d}t, \tag{11}$$

where $\overline{q}(t)$ represents the instantaneous mean boundary heat flux of the heated surfaces and τ represents the vibration period of the piezoelectric fan.

As shown in Fig. 9, when the total mesh number is larger than 2.06 million, the change of the time-averaged mean Nusselt number is less than 1%. Therefore, a mesh number of 2.06 million is chosen to perform simulations.

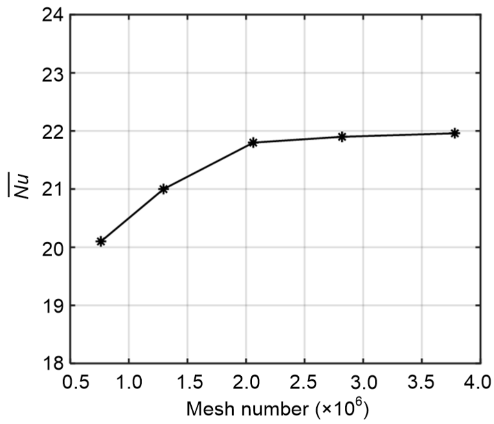

Fig. 9 Mesh independence test results

4 Results and discussion

4.1 Validation of the numerical simulations

Validations of the numerical simulations are performed by comparing the time-averaged mean Nusselt number of the numerical simulations with the experimental results, as shown in Fig. 10. The result shows that the computational results and the experiment results are in good agreement, with deviations less than 10%.

4.2 Flow structure

Fig. 11 shows the lateral velocity vectors in the cross sections of x=20, 40, 60, 80, 100, and 120 mm in the vibrating case of a=0.48 and Re=1820 at the instant t=τ/4. The lateral velocity V_{yz} is defined as

$$V_{yz}=\sqrt{v^2+w^2}. \tag{12}$$

The result illustrates that the vibration of the piezoelectric fan promotes lateral movement of the surrounding fluid and a pair of strong longitudinal vortexes is generated in the back area of the fan. In the fan length area (0<x<60 mm), due to the increase of the fan displacement, the intensity of the longitudinal vortexes increases gradually with the flow distance and reaches a maximum near the fan tip. However, in the downstream area (x>60 mm), due to the lack of lateral momentum input, the intensity of the longitudinal vortexes decreases rapidly under the effects of viscosity and wall confinement.

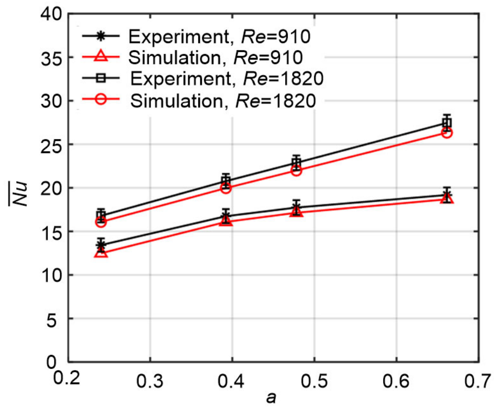

Fig. 10 Comparisons of the computed time-averaged mean Nusselt number with the experimental results

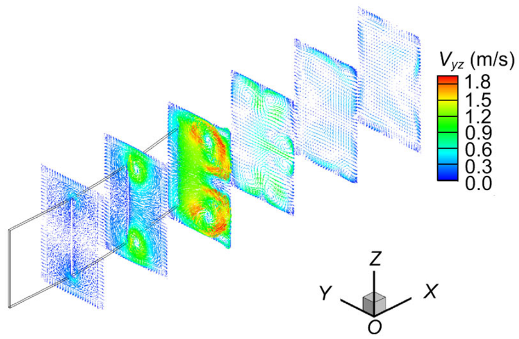

Fig. 11 Lateral velocity vectors in the cross sections of x=20, 40, 60, 80, 100, and 120 mm in the vibrating case of a=0.48 and Re=1820 at the instant t=τ/4

In order to understand the formation mechanism of the longitudinal vortexes, the instantaneous lateral velocity vectors in the cross sections of x=40 mm in the vibrating case of a=0.48 and Re=1820 at the instant t=0, τ/8, τ/4, and 3τ/8 are investigated, as shown in Fig. 12. When the piezoelectric fan is moving from the equilibrium position towards the left wall, an impinging jet flow area A is formed between the left wall and the fan surface under the push effect of the fan, as shown in Fig. 12a. In area A, due to the confinement effect of the left wall, the flow slows down gradually in the normal direction of the left wall and accelerates along the left wall. Finally, the impinging jet flow totally translates into a shear flow along the left wall towards the upper and lower walls. Similarly, due to the confinement effect of the upper and lower walls, the shear flow along the left wall will also translate into a shear flow along the upper and lower walls. Also, under the pull effect of the fan, a pull flow area B is formed between the right wall and the fan. In area B, the fluid follows the fan moving towards the left and continuously entrains ambient fluid into the motion. Because the pull flow and the shear flow along the upper and lower walls move in opposite directions, a pair of strong longitudinal vortexes V1 and V2 with oppositely revolving directions are generated on the right side of the fan tips. As shown in Fig. 12b, after passing the equilibrium position, the velocity of the piezoelectric fan decreases gradually. As a result, under the inertia effect, the normal velocity of the fluid in area B decreases and the lateral velocity along the fan surface increases. As shown in Fig. 12c, when the velocity of the piezoelectric fan decreases to zero at the instant $t=\tau/4$, on one hand, the velocity of the fluid in area A is obviously decreased. On the other hand, in area B, the normal flow towards the fan surface completely translates into a shear flow along the fan surface. At that moment, the piezoelectric fan is going to move in the opposite direction and the longitudinal vortexes V1 and V2 reach the critical state. As shown in Fig. 12d, when the piezoelectric fan is in its motion from the left to the equilibrium position, a new impinging jet flow area A2 is formed on the right side of the fan and a new pull flow area B2 is formed between the left wall and the fan. Moreover, as observed in Fig. 12d, because the motion of the piezoelectric fan hinders the rotation motion of the longitudinal vortexes V1 and V2, the intensities of V1 and V2 decrease rapidly. In the meantime, a new longitudinal vortex pair V3 and V4 begins to form on the left side of the fan tips. In conclusion, under the effects of the piezoelectric fan vibration and the wall confinement effect, two longitudinal vortex pairs are generated in one cycle, and greatly promote momentum exchange between the main flow and the near-wall flow.

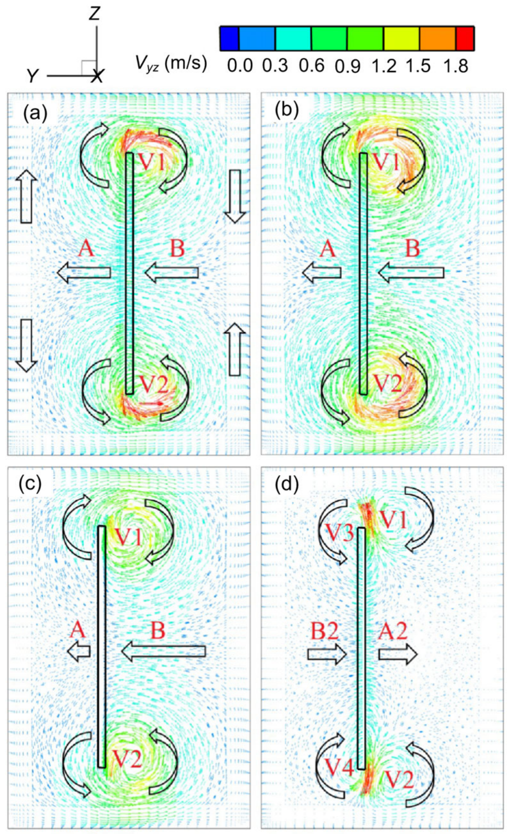

Fig. 12 Lateral velocity vectors in the cross sections of x=40 mm for the vibrating case with a=0.48 and Re=1820 at the instant t=0 (a), $t=\tau/8$ (b), $t=\tau/4$ (c), and $t=3\tau/8$ (d)

4.3 Heat transfer

In order to reveal the heat transfer enhancement mechanism induced by the piezoelectric fan, the influence of the longitudinal vortexes on the temperature field is analyzed.

Fig. 13 shows the temperature contours and velocity vectors in the cross section of x=80 mm in the stationary case and the vibrating case (a=0.48) of Re=1820 at the instant $t=\tau/4$. The dimensionless form of temperature $T_0(x, t)$ proposed by Mehryan et al. (2019) is used to facilitate the analysis:

$$T_0(x,t)=\frac{T(x,t)-T_{\mathrm{in}}}{T_{\mathrm{sur}}-T_{\mathrm{in}}}. \tag{13}$$

As shown in Fig. 13a, when the piezoelectric fan is stationary, the flow state in the channel is laminar and the flow direction is almost perpendicular to the cross section. Thus, the heat exchange between the heated walls and the center flow is very weak. As shown in

Fig. 13b, the vibration of the piezoelectric fan causes a complicated flow structure with multi-longitudinal vortexes, which take the cold fluid of the mainstream to the heated walls and take the hot fluid away from the heated walls. Consequently, for the wall area to which the cold fluid is moving, the thickness of the thermal boundary layer is obviously reduced. However, for the wall area where the heated fluid is moving away, the thickness of the thermal boundary layer is relatively increased.

Fig. 14 compares the dimensionless local boundary heat flux between the stationary case and the vibrating case (a=0.48) of Re=1820 at the instant t=τ/4 in the cross section of x=80 mm. The dimensionless local boundary heat flux is defined as

$$q_0(x,t)=\frac{q(x,t)}{\overline{q}_{\mathrm{s}}}\cdot\frac{T_{\mathrm{sur,v}}-T_{\mathrm{in}}}{T_{\mathrm{sur,s}}-T_{\mathrm{in}}},\tag{14}$$

where the subscripts v and s represent the vibrating case and the stationary case, respectively. $\overline{q}_{\mathrm{s}}$ is the mean boundary heat flux of the stationary case at t=τ/4. The marks on the x axis in Fig. 14 have been plotted in Fig. 13 and the distance between two adjacent letters is 10 mm. The result illustrates that the distribution of the dimensionless local boundary heat flux matches well with the above analysis in Fig. 13 and, as a whole, the heat exchange between the hot fluid near the heated wall and the cold fluid in the channel center is improved and the heat transfer capability of the heated surfaces is remarkably enhanced.

Fig. 15 shows the distribution of the instantaneous dimensionless local boundary heat flux ratio ($\eta(x, t)$) in the case of a=0.48 and Re=1820 at the instant t=τ/4. The definition of $\eta(x, t)$ is:

$$\eta(x,t)=\frac{q_{0,\mathrm{v}}(x,t)}{q_{0,\mathrm{s}}(x,t)}=\frac{q_{\mathrm{v}}(x,t)}{\overline{q}_{\mathrm{s}}}\cdot\frac{T_{\mathrm{sur,s}}-T_{\mathrm{in}}}{T_{\mathrm{sur,v}}-T_{\mathrm{in}}}.\tag{15}$$

The distribution of $\eta(x, t)$ in Fig. 15 shows that the local heat transfer enhancement induced by the piezoelectric fan is distributed unevenly. The local heat transfer performance can be enhanced 5–7 times near the free end of the piezoelectric fan while it decreases rapidly with the moving distance of the fluid. This observation means that it is better to use a

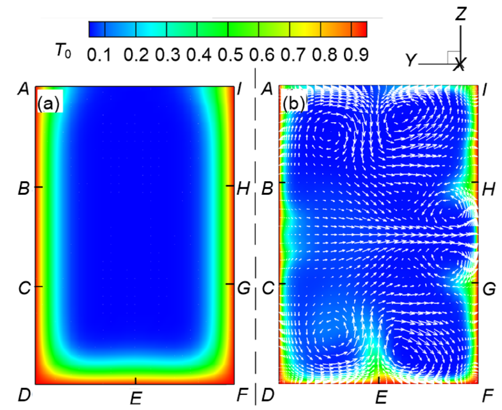

Fig. 13 Temperature contours and velocity vectors in the cross section of x=80 mm in the stationary case (a) and the vibrating case (a=0.48) of Re=1820 at t=τ/4 (b)

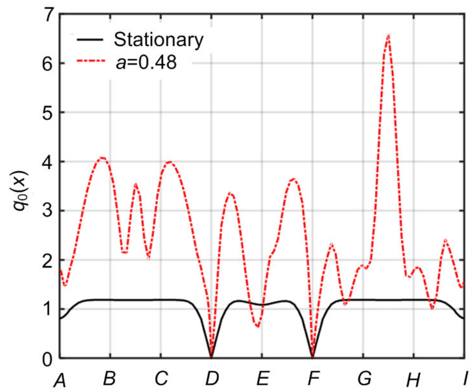

Fig. 14 Distributions of the instantaneous local boundary heat flux in the stationary case and the vibrating case (a=0.48) of Re=1820 in the cross section of x=80 mm at t=τ/4

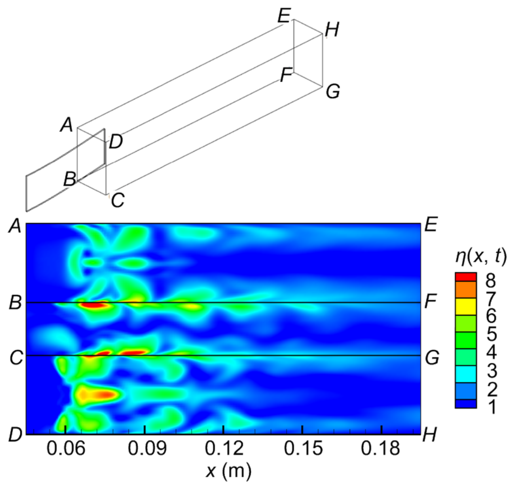

Fig. 15 Distribution of the instantaneous dimensionless local boundary heat flux ratio in the case of a=0.48 and Re=1820 at t=τ/4

piezoelectric fan to solve non-uniform heat flux problems such as hot-spot cooling or for local temperature control.

Fig. 16 shows the instantaneous mean Nusselt number ($\overline{Nu}(t)$) variations of the three heated surfaces in the vibrating case of a=0.48 and Re=1820. The description of the heated surfaces has been plotted in Fig. 15. For the front and back surfaces, $\overline{Nu}(t)$ fluctuates synchronously with the piezoelectric fan vibration with a fluctuation ratio of 4.5%, while for the bottom surface, due to symmetry, the fluctuation frequency of $\overline{Nu}(t)$ is twice the value of the piezoelectric fan and the fluctuation ratio is only 2.4%. Considering that the heat capacity in real applications will also inhibit the temperature fluctuation, it is reasonable to assume that the piezoelectric fan has a stable performance in local heat transfer enhancement.

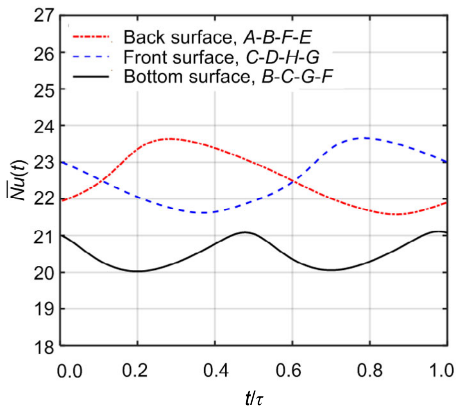

Fig. 16 Variations of the instantaneous mean Nusselt number in one period in the case of *a*=0.48 and *Re*=1820

4.4 Effects of amplitude and cross flow Reynolds number

Fig. 17 compares the temperature contours and corresponding velocity vectors between the vibrating cases of a=0.24, Re=1820 and a=0.48, Re=1820 in a cross section of x=80 mm at t=τ/4. As shown in Fig. 17a, in the case of a=0.24, the intensity of the longitudinal vortexes generated by the piezoelectric fan is too low to cause apparent rotation of the fluid near the channel walls. As a result, the momentum and heat exchanges mainly concentrate in the channel center and the thermal boundary layers are relatively thick. However, when the dimensionless amplitude increases to 0.48, as shown in Fig. 17b, the longitudinal vortexes become stronger and the distance between the vortex cores and the channel walls is decreased. Consequently, the heat exchange between the main flow and the near-wall flow is promoted and the heat transfer performance of the heated surfaces is significantly enhanced. According to the experimental results, compared with the stationary case, the time-averaged mean Nusselt number ($\overline{Nu}$) is enhanced by 83.2% in the case of a=0.48 and Re=1820, while it is only enhanced by 34.5% in the case of a=0.24 and Re=1820.

Fig. 18 compares the distributions of the local boundary heat flux ratio between the vibrating cases of a=0.48, Re=910 and a=0.48, Re=1820 at the instant t=τ/4. The result illustrates that, in the case of Re=910, the enhancement of the heat transfer performance mainly distributes near the free end of the piezoelectric fan and the downstream area of the channel is relatively less affected. The cause for this phenomenon is that the convection intensity along the flow direction is weak and the axial velocity of the vortexes is small for the low Re case. Therefore, the vortexes tend to move laterally, which exacerbates the wall confinement effect and accelerates the vorticity dissipation. As a result, with further amplitude increasing, the increment speed of $\overline{Nu}$ is decelerated significantly. However, when Re increases to 1820, due to the enhanced convection intensity, the axial velocity of the vortexes is increased and the vortexes can move further along the flow direction. Consequently, the enhanced heat transfer performance is distributed more uniformly and the increment speed of $\overline{Nu}$ with fan amplitude is maintained. According to the experimental results, in the case of Re=1820, when a is increased from 0.48 to 0.66, the enhancement ratio of $\overline{Nu}$ rises from 83.2% to 119.9%. However, in the case of Re=910, when a is increased from 0.48 to 0.66, the enhancement ratio of $\overline{Nu}$ only rises from 84.5% to 99.5%.

4.5 Pressure drop

Limited by the experimental conditions, the pressure drop in this study is too small to measure. Thus, the pressure drop here is investigated based on the simulation results.

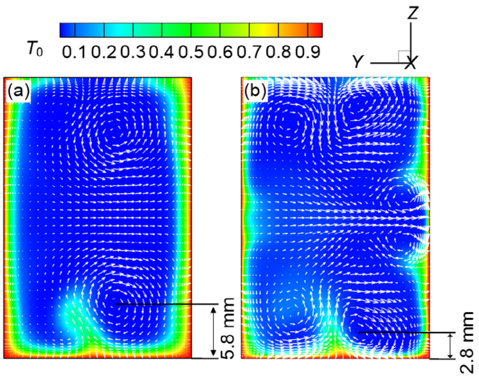

Fig. 17 Temperature contours and velocity vectors for the vibrating cases in the cross section of *x*=80 mm in the vibrating cases (*Re*=1820) of *a*=0.24 (a) and *a*=0.48 (b) at *t*=*τ*/4

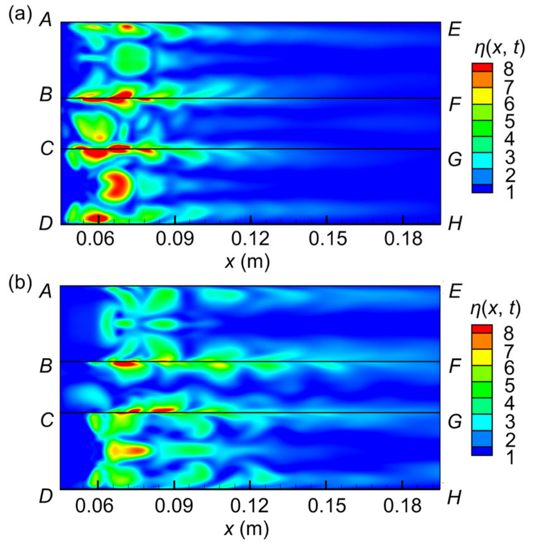

Fig. 18 Distributions of the dimensionless local boundary heat flux ratio in the vibrating cases (*a*=0.48) of *Re*=910 (a) and *Re*=1820 (b) at *t*=*τ*/4

Fig. 19 compares the pressure drop (Δp) of the channel between the stationary case and a=0.24 and a=0.48 cases with Re=1820. The result shows that the piezoelectric fan's vibration has less effect on the pressure drop of the channel. Compared with the stationary case, the piezoelectric fan operated at a=0.48 and Re=1820 only enhances the pressure drop by 12.5%. This phenomenon is explained as follows:

The viscous dissipation function of a Newtonian fluid in a laminar channel is

$$\Phi=\mu\left[2\left(\frac{\partial u}{\partial x}\right)^2+2\left(\frac{\partial v}{\partial y}\right)^2+2\left(\frac{\partial w}{\partial z}\right)^2+\left(\frac{\partial u}{\partial y}+\frac{\partial v}{\partial x}\right)^2+\left(\frac{\partial u}{\partial z}+\frac{\partial w}{\partial x}\right)^2+\left(\frac{\partial v}{\partial z}+\frac{\partial w}{\partial y}\right)^2\right]. \tag{16}$$

For laminar flow in a channel, $u\gg v$, $u\gg w$ and $\partial/\partial x\ll\partial/\partial y$, $\partial/\partial x\ll\partial/\partial z$. Therefore, Eq. (16) can be simplified as

$$\Phi\approx\mu\left[\left(\frac{\partial u}{\partial y}\right)^2+\left(\frac{\partial u}{\partial z}\right)^2\right]. \tag{17}$$

Eq. (17) shows that the flow resistance of the channel mainly depends on the velocity of the main flow. Because the longitudinal vortexes mainly change the lateral velocity, the piezoelectric fan's vibration has a low effect on the flow resistance.

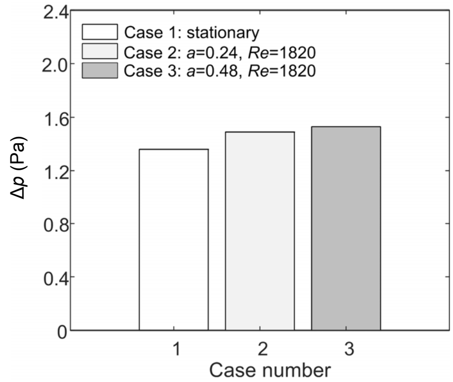

Fig. 19 Pressure drop of the channel

From the analysis above, the main price of using piezoelectric fan comes from its power consumption (37 mW for a=0.66). Considering the real-time adjustability of the piezoelectric fan, its real power consumption is related to its running time, so it is better to use a piezoelectric fan as an assistive device to solve the hot-spot problem or the local temperature control problem in electronic cooling systems.

5 Conclusions

The present work experimentally and numerically investigates the local heat transfer enhancement induced by a piezoelectric fan with cross flow in a local heated channel. Main findings from the study are as follows:

1. A vibrating piezoelectric fan can substantially improve the local cooling performance of the channel. Compared with the stationary case, the piezoelectric fan operated at a=0.66 and Re=1820 enhances the time-averaged mean Nusselt number ($\overline{Nu}$) by as much as 119.9%.

2. The heat transfer enhancement mainly comes from the longitudinal vortex pairs generated by the piezoelectric fan, which greatly promote the heat exchange between the hot fluid near the heated walls and the cold fluid in the main flow.

3. The piezoelectric fan's vibration has less effect on the pressure drop of the channel. In the case of a=0.48 and Re=1820, the pressure drop is only increased by 12.5%.

Based on the results presented above, the piezoelectric fan has good prospects for local heat transfer enhancement. It allows the cooling circuit to be operated at lower mass flow rate while keeping the hot-spot area working safely. Future studies will further investigate the interaction between the mainstream and the piezoelectric fan by presenting more visualization work. Moreover, more parametric investigations should be conducted to figure out the main parameters and develop mathematical models.

Contributors

Yun-long QIU performed the experimental tests and numerical simulations. Chang-ju WU processed the corresponding data. Wei-fang CHEN helped to organize the manuscript.

Conflict of interest

Yun-long QIU, Chang-ju WU, and Wei-fang CHEN declare that they have no conflict of interest.

References

Abdullah MK, Abdullah MZ, Ramana MV, et al., 2009. Numerical and experimental investigations on effect of fan height on the performance of piezoelectric fan in microelectronic cooling. *International Communications in Heat and Mass Transfer*, 36(1):51-58. https://doi.org/10.1016/j.icheatmasstransfer.2008.08.017

Abdullah MK, Ismail NC, Abdullah MZ, et al., 2012a. Effects of tip gap and amplitude of piezoelectric fans on the performance of heat sinks in microelectronic cooling. *Heat and Mass Transfer*, 48(6):893-901. https://doi.org/10.1007/s00231-011-0944-z

Abdullah MK, Ismail NC, Mujeebu MA, et al., 2012b. Optimum tip gap and orientation of multi-piezofan for heat transfer enhancement of finned heat sink in microelectronic cooling. *International Journal of Heat and Mass Transfer*, 55(21-22):5514-5525. https://doi.org/10.1016/j.ijheatmasstransfer.2012.05.024

Açikalin T, Wait SM, Garimella SV, et al., 2004. Experimental investigation of the thermal performance of piezoelectric fans. *Heat Transfer Engineering*, 25(1):4-14. https://doi.org/10.1080/01457630490248223

Açikalin T, Garimella SV, Raman A, et al., 2007. Characterization and optimization of the thermal performance of miniature piezoelectric fans. *International Journal of Heat and Fluid Flow*, 28(4):806-820. https://doi.org/10.1016/j.ijheatfluidflow.2006.10.003

Alsabery AI, Saleh H, Ghalambaz M, et al., 2019. Fluid-structure interaction analysis of transient convection heat transfer in a cavity containing inner solid cylinder and flexible right wall. *International Journal of Numerical Methods for Heat & Fluid Flow*, 29(10):3756-3780. https://doi.org/10.1108/HFF-10-2018-0593

Arshad A, Jabbal M, Yan YY, 2020. Synthetic jet actuators for heat transfer enhancement–a critical review. *International Journal of Heat and Mass Transfer*, 146:118815. https://doi.org/10.1016/j.ijheatmasstransfer.2019.118815

Deng X, Luo ZB, Xia ZX, et al., 2019. Experimental investigation on the flow regime and impingement heat transfer of dual synthetic jet. *International Journal of Thermal Sciences*, 145:105864. https://doi.org/10.1016/j.ijthermalsci.2019.02.039

Fairuz ZM, Sufian SF, Abdullah MZ, et al., 2014. Effect of piezoelectric fan mode shape on the heat transfer characteristics. *International Communications in Heat and Mass Transfer*, 52:140-151. https://doi.org/10.1016/j.icheatmasstransfer.2013.11.013

Ghalambaz M, Jamesahar E, Ismael MA, et al., 2017. Fluid-structure interaction study of natural convection heat transfer over a flexible oscillating fin in a square cavity. *International Journal of Thermal Sciences*, 111:256-273. https://doi.org/10.1016/j.ijthermalsci.2016.09.001

Ghalambaz M, Mehryan SAM, Izadpanahi E, et al., 2019a. MHD natural convection of Cu–Al_2O_3 water hybrid nanofluids in a cavity equally divided into two parts by a vertical flexible partition membrane. *Journal of Thermal Analysis and Calorimetry*, 138(2):1723-1743. https://doi.org/10.1007/s10973-019-08258-w

Ghalambaz M, Chamkha AJ, Wen DS, 2019b. Natural convective flow and heat transfer of Nano-Encapsulated Phase Change Materials (NEPCMs) in a cavity. *International Journal of Heat and Mass Transfer*, 138:738-749. https://doi.org/10.1016/j.ijheatmasstransfer.2019.04.037

Ghalambaz M, Doostani A, Izadpanahi E, et al., 2020. Conjugate natural convection flow of Ag–MgO/water hybrid nanofluid in a square cavity. *Journal of Thermal Analysis and Calorimetry*, 139(3):2321-2336. https://doi.org/10.1007/s10973-019-08617-7

Guo ZZ, He ZQ, Zhao WW, et al., 2018. Efficient mesh deformation and flowfield interpolation method for unstructured mesh. *Acta Aeronautica et Astronautica Sinica*, 39(12):126-137 (in Chinese).

Hales A, Jiang X, 2018. A review of piezoelectric fans for low energy cooling of power electronics. *Applied Energy*, 215:321-337.
https://doi.org/10.1016/j.apenergy.2018.02.014

Jamesahar E, Sabour M, Shahabadi M, et al., 2020. Mixed convection heat transfer by nanofluids in a cavity with two oscillating flexible fins: a fluid–structure interaction approach. *Applied Mathematical Modelling*, 82:72-90.
https://doi.org/10.1016/j.apm.2019.12.018

Jeng TM, Liu CH, 2015. Moving-orientation and position effects of the piezoelectric fan on thermal characteristics of the heat sink partially filled in a channel with axial flow. *International Journal of Heat and Mass Transfer*, 85: 950-964.
https://doi.org/10.1016/j.ijheatmasstransfer.2015.02.053

Jiang ZZ, Chen WF, Zhao WW, 2018. Numerical analysis of the micro-Couette flow using a non-Newton–Fourier model with enhanced wall boundary conditions. *Microfluidics and Nanofluidics*, 22(10), Article No. 10.
https://doi.org/10.1007/s10404-017-2028-y

Kimber M, Garimella SV, 2009. Cooling performance of arrays of vibrating cantilevers. *Journal of Heat Transfer*, 131(11):111401.
https://doi.org/10.1115/1.3153579

Kurnia JC, Sasmito AP, Mujumdar AS, 2011. Evaluation of the heat transfer performance of helical coils of non-circular tubes. *Journal of Zhejiang University-SCIENCE A (Applied Physics & Engineering)*, 12(1):63-70.
https://doi.org/10.1631/jzus.A1000296

Lee YJ, Singh PK, Lee PS, 2015. Fluid flow and heat transfer investigations on enhanced microchannel heat sink using oblique fins with parametric study. *International Journal of Heat and Mass Transfer*, 81:325-336.
https://doi.org/10.1016/j.ijheatmasstransfer.2014.10.018

Li XJ, Zhang JZ, Tan XM, 2017. Convective heat transfer on a flat surface induced by a vertically-oriented piezoelectric fan in the presence of cross flow. *Heat and Mass Transfer*, 53(9):2745-2768.
https://doi.org/10.1007/s00231-017-2019-2

Li XJ, Zhang JZ, Tan XM, 2018a. Effects of piezoelectric fan on overall performance of air-based micro pin-fin heat sink. *International Journal of Thermal Sciences*, 126: 1-12.
https://doi.org/10.1016/j.ijthermalsci.2017.12.018

Li XJ, Zhang JZ, Tan XM, 2018b. An investigation on convective heat transfer performance around piezoelectric fan vibration envelope in a forced channel flow. *International Journal of Heat and Mass Transfer*, 126:48-65.
https://doi.org/10.1016/j.ijheatmasstransfer.2018.06.021

Lin CN, 2013. Enhanced heat transfer performance of cylindrical surface by piezoelectric fan under forced convection conditions. *International Journal of Heat and Mass Transfer*, 60:296-308.
https://doi.org/10.1016/j.ijheatmasstransfer.2013.01.034

Liu SF, Huang RT, Sheu WJ, et al., 2009. Heat transfer by a piezoelectric fan on a flat surface subject to the influence of horizontal/vertical arrangement. *International Journal of Heat and Mass Transfer*, 52(11-12):2565-2570.
https://doi.org/10.1016/j.ijheatmasstransfer.2009.01.013

Ma HK, Su HC, Liu CL, et al., 2012. Investigation of a piezoelectric fan embedded in a heat sink. *International Communications in Heat and Mass Transfer*, 39(5): 603-609.
https://doi.org/10.1016/j.icheatmasstransfer.2012.03.003

Mehryan SAM, Izadpanahi E, Ghalambaz M, et al., 2019. Mixed convection flow caused by an oscillating cylinder in a square cavity filled with Cu-Al_2O_3/water hybrid nanofluid. *Journal of Thermal Analysis and Calorimetry*, 137(3):965-982.
https://doi.org/10.1007/s10973-019-08012-2

Moffat RJ, 1988. Describing the uncertainties in experimental results. *Experimental Thermal and Fluid Science*, 1(1): 3-17.
https://doi.org/10.1016/0894-1777(88)90043-X

Peles Y, Koşar A, Mishra C, et al., 2005. Forced convective heat transfer across a pin fin micro heat sink. *International Journal of Heat and Mass Transfer*, 48(17): 3615-3627.
https://doi.org/10.1016/j.ijheatmasstransfer.2005.03.017

Sufian SF, Abdullah MZ, Mohamed JJ, 2013. Effect of synchronized piezoelectric fans on microelectronic cooling performance. *International Communications in Heat and Mass Transfer*, 43:81-89.
https://doi.org/10.1016/j.icheatmasstransfer.2013.02.013

Wait SM, Basak S, Garimella SV, et al., 2007. Piezoelectric fans using higher flexural modes for electronics cooling applications. *IEEE Transactions on Components and Packaging Technologies*, 30(1):119-128.
https://doi.org/10.1109/TCAPT.2007.892084

Wang XQ, Mujumdar AS, 2007. Heat transfer characteristics of nanofluids: a review. *International Journal of Thermal Sciences*, 46(1):1-19.
https://doi.org/10.1016/j.ijthermalsci.2006.06.010

Wen DS, Lin GP, Vafaei S, et al., 2009. Review of nanofluids for heat transfer applications. *Particuology*, 7(2):141-150.
https://doi.org/10.1016/j.partic.2009.01.007

Xia CC, Chen WF, 2016. Boundary-layer transition prediction using a simplified correlation-based model. *Chinese Journal of Aeronautics*, 29(1):66-75.
https://doi.org/10.1016/j.cja.2015.12.003

Xu Y, Moon C, Wang JJ, et al., 2019. An experimental study on the flow and heat transfer of an impinging synthetic jet. *International Journal of Heat and Mass Transfer*, 144: 118626.
https://doi.org/10.1016/j.ijheatmasstransfer.2019.118626

Yeom T, Simon TW, North M, et al., 2016. High-frequency translational agitation with micro pin-fin surfaces for enhancing heat transfer of forced convection. *International Journal of Heat and Mass Transfer*, 94:354-365.
https://doi.org/10.1016/j.ijheatmasstransfer.2015.11.054

中文概要

题　目：压电风扇对管内局部受迫对流换热的强化效果研究

目　的：电子设备的局部过热问题对散热系统的设计提出了新的考验。针对传统被动式散热技术调节困难、调节代价大等问题，本文提出使用压电风扇作为控制元件对管内局部过热区域进行主动对流换热效果强化的方案，期望通过实验与数值模拟研究掌握压电风扇在管内横流作用下的流动控制特性及强化传热机理，为压电风扇在实际工程中的应用提供理论指导。

创新点：1. 通过基于等温设计的实验系统测试加热面在压电风扇作用下的时均努塞尔数，并证明压电风扇对管内局部区域对流换热效果的强化能力；2. 通过数值模拟分析压电风扇的纵向涡产生特性并解释纵向涡对局部对流换热效果的强化机理。

方　法：1. 利用铜热沉导热快、热容大等特性建立定常的等温换热面，并测量得到等温壁面在压电风扇作用下的时均努塞尔数；2. 使用基于动网格技术的数值模拟，得到压电风扇作用下的流场与温度场信息，分析压电风扇的流动控制特性，并解释压电风扇强化局部对流换热的机理；3. 通过参数化研究说明振幅和来流雷诺数对压电风扇强化对流换热效果的影响。

结　论：1. 压电风扇的振动可以显著地强化管内局部区域的对流换热性能；2. 压电风扇引起的对流换热强化主要来自其振动产生的纵向涡对；3. 压电风扇的振动对管内流动压降的影响较小。

关键词：压电风扇；局部对流换热强化；受迫对流；纵向涡；压降